

UNIVERSIDAD SAN FRANCISCO DE QUITO USFQ

Colegio de Ciencias e Ingeniería

**X ray tomography applied in
archaeological artefacts using phase shift
imaging technique**

Angelo Saavedra Mafla

Física

Trabajo de titulación presentado como requisito
para la obtención del título de

Licenciado en Física

Diciembre 21, 2023

UNIVERSIDAD SAN FRANCISCO DE QUITO USFQ

Colegio de Ciencias e Ingeniería

**HOJA DE CALIFICACIÓN DE TRABAJO DE FIN DE
CARRERA**

Angelo Saavedra Mafla

Nombre del profesor, Título académico: Melissa Infusino, PhD

Diciembre 21, 2023

© Derechos de Autor

Por medio del presente documento certifico que he leído todas las Políticas y Manuales de la Universidad San Francisco de Quito USFQ, incluyendo la Política de Propiedad Intelectual USFQ, y estoy de acuerdo con su contenido, por lo que los derechos de propiedad intelectual del presente trabajo quedan sujetos a lo dispuesto en esas Políticas.

Asimismo, autorizo a la USFQ para que realice la digitalización y publicación de este trabajo en el repositorio virtual, de conformidad a lo dispuesto en la Ley Orgánica de Educación Superior del Ecuador.

Nombres y apellidos: Angelo Saavedra Mafla

Código: 00209253

Cédula de Identidad: 1723366868

Lugar y fecha: Diciembre 21, 2023

ACLARACIÓN PARA LA PUBLICACIÓN

Nota: El presente trabajo, en su totalidad o cualquiera de sus partes, no debe ser considerado como una publicación, incluso a pesar de estar disponible sin restricciones a través de un repositorio institucional. Esta declaración se alinea con las prácticas y recomendaciones presentadas por el Committee on Publication Ethics COPE descritas por Barbour et al. (2017) Discussion document on best practice for issues around theses publishing, disponible en <http://bit.ly/COPETHeses>

UNPUBLISHED DOCUMENT

Note: The following capstone project is available through Universidad San Francisco de Quito USFQ institutional repository. Nonetheless, this project – in whole or in part – should not be considered a publication. This statement follows the recommendations presented by the Committee on Publication Ethics COPE described by Barbour et al. (2017) Discussion document on best practice for issues around theses publishing available on <http://bit.ly/COPETHeses>

Agradecimientos

A mi familia que siempre estuvo ahí para apoyarme en los éxitos y en los fracasos. Me dieron la fuerza para seguir intentando aun cuando era muy fácil rendirse. A mis compañeros que me ayudaron más de lo que era necesario, en especial a Martín y Tefa. Nada de esto hubiera sido posible sin ustedes. Al club de debate, que me dieron la motivación para seguir soñando y alcanzar éxitos que nunca hubiera imaginado posible antes.

Resumen

Las técnicas de imagen por contraste de fase son un método más preciso para reconstruir muestras de bajo número atómico y poder analizar sus datos. Mediante el uso de la transformada de Hough en 3D, se descubrió que la cerámica ecuatoriana de la region Jama Coaque exhibía patrones paralelos en su distribución de sus poros, lo que implica que se asemejan bastante a las técnicas de enrollado que todavía son populares hoy en día. Más del 60 por ciento de los poros en cada muestra estaban en el rango de $100\mu m^2$ a $2400\mu m^2$, lo que sugiere una clara intención en sus técnicas de mantener poros más pequeños y eliminar los grandes, ya que son una anomalía.

Keywords: *Técnicas de enrollado, poros pequeños*

Abstract

Phase contrast imaging techniques are a more precise method of reconstructing low atomic number samples and therefore analyzing their data. Using the 3D Hough transform, it was found that Ecuadorean ceramic that dates back to 355 a.C. exhibited parallel patterns in their pore distribution that assimilate quite closely to coiling techniques that are still popular even now. More than 60 percent of pores for each sample were in the range of $100\mu m^2$ to $2400\mu m^2$ which suggests a clear intention in their techniques to remain with smaller pores and eliminate big ones, as they are an anomaly.

Keywords: *Coiling techniques, smaller pores*

Contents

1	Introduction	14
1.0.1	Motivation	14
1.0.2	Computed Tomography	15
1.0.3	Phase Contrast Imaging	20
1.0.4	Voxels	24
1.0.5	Hough transform	25
2	Methodology	32
2.0.1	Experimental Set Up	32
2.0.2	Cone Beam Geometry	36
2.0.3	Crystal Interferometry	38

	9
2.0.4 AVIZO Reconstruction Program	41
2.0.5 Hough Transform	42
3 Results	44
3.0.1 Hough Lines	51
4 Conclusions	56
Bibliography	58
A Histogram graphs of ceramic samples	62
B Box and whisker plots of ceramic samples	64
C Hough lines and parallelism	66

List of Figures

1.1	X-ray's interaction with matter [1]	18
1.2	Differences between standard techniques (left) and phase contrast techniques (right) [2]	21
1.3	Phase Contrast Experimental Set Up [2]	22
1.4	Coherent waves [3]	23
1.5	Phase Contrast Detector [4]	24
1.6	Voxel	25
1.7	Hough Transform [5]	26
1.8	Multiple Hough transforms [5]	26
1.9	Line detection algorithm [5]	27
1.10	Parametrization of a line [6]	28

	11
1.11 Sinusoidal Hough transform [5]	29
1.12 Representation of θ and ϕ [7]	30
1.13 The relationship between x' , y' and \vec{b} [7]	31
2.1 Experimental Set Up [8]	33
2.2 Ceramic Figures	35
2.3 Cone Beam X-ray Source [8]	37
2.4 Crystal Interferometry [9]	39
2.5 Bragg's Condition	40
2.6 Example Of Avizo Reconstruction [8]	41
2.7 Hough lines of Coiling technique (top) and circular techniques (bottom)	43
3.1 Reconstructed pieces with visible porosity	44
3.2 Pore Visualization of sample 12 (left) and sample 11(right)	46
3.3 Volume Histogram of sample 12 ($27000\mu m^3$)	47
3.4 Volume Histogram of sample 11 ($1000\mu m^3$)	48
3.5 Histogram Sample 15 $1000\mu m^3$	48

	12
3.6 Volume Box Plot of sample 12	49
3.7 Volume Box Plot of sample 11	50
3.8 Sample 15 box and Whisker Plot	50
3.9 Sample 12 Hough Lines	52
3.10 Sample 11 Hough Lines	52
3.11 Sample 15 Hough Lines	53
3.12 Parallelism Sample 12	54
3.13 Parallelism Sample 11	54
3.14 Parallelism Sample 15	55
A.1 Histogram Sample 7	62
A.2 Histogram Sample 13	63
B.1 Histogram Sample 13	64
B.2 Histogram Sample 7	65
C.1 Ceramic sample 7	66
C.2 Hough lines sample 7	67

	13
C.3 Ceramic Sample 13	67
C.4 Hough lines sample 13	68
C.5 Parallelism Sample 13	69
C.6 Parallelism Sample 7	69

Chapter 1

Introduction

1.0.1 Motivation

Ecuador has a rich history in artefacts, cultures and ancient civilizations and any exploration of its past is vital to understanding more about our present. Last year in 2022, the anthropology career of USFQ excavated different areas of the Jama Coaque region and brought back multiple samples of ceramics to be studied, however, it was still unclear for them what time periods these samples were from. Equally, due to a lack of non invasive techniques available to them, the microscopic information within these samples couldn't be analyzed. Because of this, I was given the opportunity to go to the research institute (CNR) in Napoli, Italy to investigate, in collaboration with Anthropology, porosity distribution and its volume on the ceramics of the Jama Coaque region. We did this by using Computer tomography scans, which have the unique ability to undergo non destructive

techniques to analyze the internal structures, like porosity, of ceramic materials. This is hugely important for archaeology, especially for factors like preservation, which allows multiple studies to be done on a single object without having to destroy or break any piece. This region is estimated to have been around from 1500 BC until 500 AD and were especially known to have large collections of ceramics that they would use to trade to other regions[10]. That is why I think it would be interesting to analyze its pore distribution and obtain microscopic data that could be useful for anthropologists to gain further insights in the reality of this region.

1.0.2 Computed Tomography

Computed tomography is an imaging procedure that utilizes the unique properties of X-rays and its interactions with materials in order to create multiple cross sectional images of an object and virtually reconstruct it in 3 dimensions [2]. CT scans function by employing contrast techniques, which have been popular since the discovery of X-rays by Wilhelm Conrad Röntgen in 1895 [9]. Their ability to penetrate almost any material meant that there could exist images of the inner structures of any object, living or non living and therefore becoming an important tool in various fields such as medicine, archaeology, geology and many others. Similarly, the low dosage of radiation that such equipment expose on humans, meant that various work could be done with relatively low harm [11]. This work was further explored by Frits Zernike in 1933 by working with diffraction gratings in order to amplify the resolution of the X-ray images. His work set the foundations for different mechanisms that would develop different phase contrast techniques

that we use in modern day, winning him the Nobel prize in Physics in 1953 [2].

X-rays are electromagnetic waves that operate at wavelengths between 0.1nm-10nm. Therefore, we know that they must obey Maxwell's laws and consequently D'Alembert equations:

$$\left(\frac{1}{c^2} \frac{\partial^2}{\partial t^2} - \nabla^2\right) \vec{E}(x, y, z, t) = 0 \quad (1.1)$$

$$\left(\frac{1}{c^2} \frac{\partial^2}{\partial t^2} - \nabla^2\right) \vec{B}(x, y, z, t) = 0 \quad (1.2)$$

This tells us that electromagnetic disturbances propagate as waves in a vacuum [11]. However, the way a wave functions in the vacuum is very different to the way it functions when it interacts with a material. This is because we have to take into account the complex refractive index of the wave, we express it with the following equation [12] :

$$n = 1 - \delta + i\beta \quad (1.3)$$

Where δ describes how the real part changes and the imaginary factor β describes how the absorption of the wave changes as it interacts with materials.

We can see this more clearly if we take a monochromatic plane wave in the vacuum with no polarization propagating in the z direction, being able to express

the wave function as:

$$\Psi(z) = E_0 e^{ikz} \quad (1.4)$$

When it interacts with a material, the angular wavenumber k is now changed to nk , where we can replace the equation of the refractive index here.

$$\Psi(z) = E_0 e^{inkz} = E_0 e^{i(1-\delta)kz} e^{-\beta kz} \quad (1.5)$$

We know that the way e^{-z} behaves is as a decaying exponential and β determines the reduction of the amplitude factor of E_0 . Similarly, we can see that δ only changes the wave function's phase by its factor.

We can see the relationship between the total change in phase of a wave and the propagating distance with [12]:

$$\Phi(z) = \int_0^z \frac{2\pi\delta(z')}{\lambda} dz'$$

Where λ is the wavelength of the X-ray wave.

This relationship can be viewed better in the following figure:

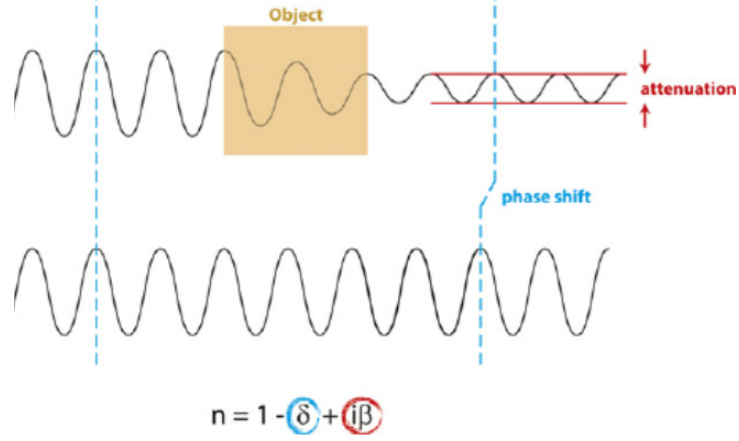


Figure 1.1: X-ray's interaction with matter [1]

Where we can see how the wave's intensity diminished and changes its phase after interacting with matter. To analyze the phase shift, we want to reduce absorption effects on the wave so that the only effect that is visible is change of phase of various points along the wave. We write the incident Electric field [12]:

$$E_i = E_0 e^{i(\omega_0 t - kz)} \hat{x} \quad (1.6)$$

Where the wave will be phase shifted by a distance of $\Phi(x, y)$ by the medium. If we assume that the phase shifts are very minimal, we can neglect the refractive effects for every X-ray wave. This helps us to express the electric field as:

$$E_{PM} = E_0 e^{i(\omega_0 t - kz + \Phi)} \hat{x} \quad (1.7)$$

Where E_{PM} is the phase shift that the medium causes onto the wave.

We can think of this effect as multiple smaller waves superimposing onto each other, each with their own phase shift $\phi_i(x, y)$.

$$E_{PM} = \frac{E_0}{A_0} \int \int_{(x,y)} e^{i(\omega_0 t - kz + \phi(x,y))} \hat{x} dx dy \quad (1.8)$$

A_0 is a normalization constant. Since we assumed that the phase shifts are relatively small, we can expand the exponential in the integral to first order such that:

$$E_{PM} = \frac{E_0 e^{i(\omega_0 t - kz)}}{A_0} \hat{x} \int \int_{(x,y)} (1 + i\phi(x, y)) dx dy \quad (1.9)$$

$$\hat{x} E_0 \left[\cos(\omega_0 t - kz) - \frac{\tilde{\phi} \sin(\omega_0 t - kz)}{A_0} + i \left(\frac{\tilde{\phi}}{A_0} \cos(\omega_0 t - kz) + \sin(\omega_0 t - kz) \right) \right] \quad (1.10)$$

We represent the integral of all small changes of the phase with $\tilde{\phi} = \int_{(x,y)} \phi(x, y) dx dy$ and define it as a phase object [12]. The unshifted wave is represented by $(\omega_0 t - kz)$ where we see a real part and an imaginary part. The only portion that we need is the real part, as we saw before with the refractive index, that is what controls the phase shift.

$$E_{RPM} = \hat{x} E_0 \left(\cos(\omega_0 t - kz) - \frac{\tilde{\phi} \sin(\omega_0 t - kz)}{A_0} \right)$$

Where E_{RPM} represents the real part of the phase shift done by the medium onto the wave. If we shift the term by $\frac{\pi}{2}$ that is not dependant on all of the small changes of the phase $\tilde{\phi}$, the *cos* changes to *sin* and we get:

$$E_{RPM} = \hat{x}E_0 \left(1 - \frac{\tilde{\phi}}{A_0} \right) \sin(\omega_0 t - kz)$$

This allows us to see that the changes in the phase due to the phase object $\tilde{\phi}$ are now converted to the changes in amplitude of the X-ray wave. This is because the intensity of the wave is proportional to the electric field squared [9], as can be shown:

$$I \propto |E_{RPM}|^2$$

Since the detectors pick up intensity peaks, this allows us to detect the phase contrast in the image and gather useful data for the reconstruction.

1.0.3 Phase Contrast Imaging

Both phase and attenuation effects don't always apply for all material nor is it easily accessible to measure them. Due to the technical difficulties involved in measuring the changes in phases standard X-ray imaging techniques only focus on measuring the attenuation contrast [?]. This is because measuring the intensity and absorption of the wave is easier, as it can be done directly with a detector,

whilst it requires additional technology and resources to be able to measure changes in the phases with the information of intensity. However, standard scans are 3 orders of magnitude less precise([2]) than phase contrast techniques and suffer from a very great limitation, which is that in order to measure the attenuation of the wave, the wave needs to pass through different atomic materials in order to produce that contrast in its absorption coefficient[2]. This doesn't happen when you have samples that consist of similar atomic number Z or low atomic numbers, as the contrast in absorption between carbon and oxygen is very little, whilst the contrast between carbon and calcium is significantly more noticeable. This is because the wave doesn't experience noticeable differences in its attenuation with similar materials and therefore appearing to be constant throughout. This presents a problem, standard techniques could observe broken bones, but could not observe the appearance of cancer cells or problems within soft tissue in the human body, as they share very similar atomic numbers. Phase contrast solves this problem, since it is significantly more sensitive to higher densities of atoms within the sample rather than their atomic number, therefore being able to visualize internal structures that otherwise wouldn't be apparent [9]. You can see this in fig 2:

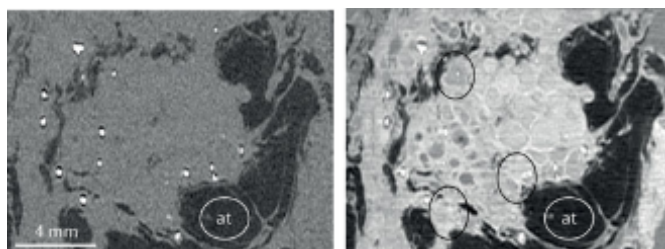


Figure 1.2: Differences between standard techniques (left) and phase contrast techniques (right) [2]

where the left picture shows attenuation contrast while the right picture displays the phase contrast on breast cells, being able to see an increase in optical resolution on low atomic number samples. In all instances, phase contrast techniques have very similar set ups, they involve having a x-ray source, which is often produced by the acceleration of electrons, the object in place and a detector which records intensity patterns. After a ray is emitted and recorded, the system rotates in order to take multiple 2D scans of each possible angle of the object, creating a contrast of the phase between these scans and successfully reconstructing this object to 3D in the computer. Depending on the experimental need, either the object rotates or the source and detector rotate while keeping the object still. This set up can be better viewed in figure 3. With the right equipment, phase contrast techniques have been shown to measure up to nanometers of a particular sample([12]).

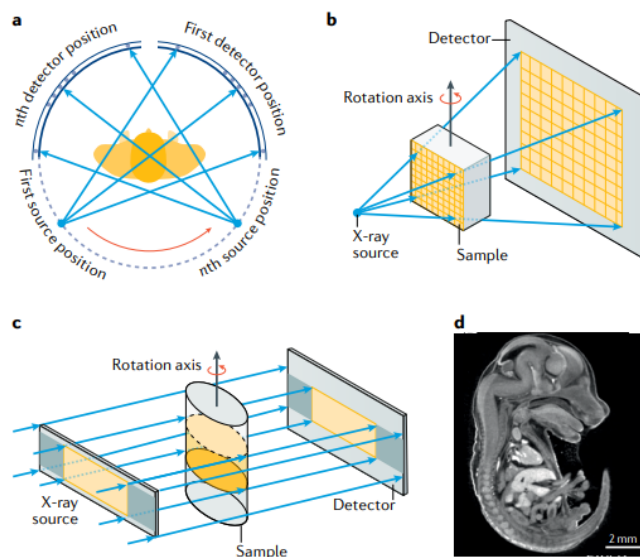


Figure 1.3: Phase Contrast Experimental Set Up [2]

The X-rays going into this phase contrast techniques need to be coherent, which means that we need constant phase difference and frequency for the incoming x-ray wave. This is important because there needs to be a constant parameter to which we can measure the contrast of the wave after it has passed a material and reached the detector. If the wave wasn't coherent, then it would be hard to properly dictate what changes are actually happening to the wave as it passes a material, an example of this is shown below:

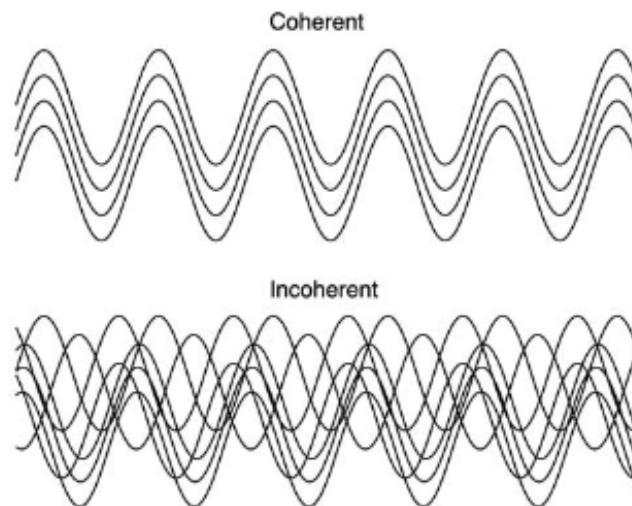


Figure 1.4: Coherent waves [3]

Once the data is successfully scanned by the phase contrast, it undergoes a series of mechanisms in order to be reconstructed digitally in the computer. The detector cannot actively measure phase shifts as their shifts don't always vary by much and it becomes very complex to truly measure the phases of each wave[2]. In order to bypass this problem, the detector measures intensity peaks and droughts. However, the information that gets to the detector is only that of X-rays and

therefore it has to use a scintillator to turn the radioactive waves into photons of wavelength of visible light and through metal oxides in a photodiode, turn the visible photons into electrons that can be properly processed by the computer[13].

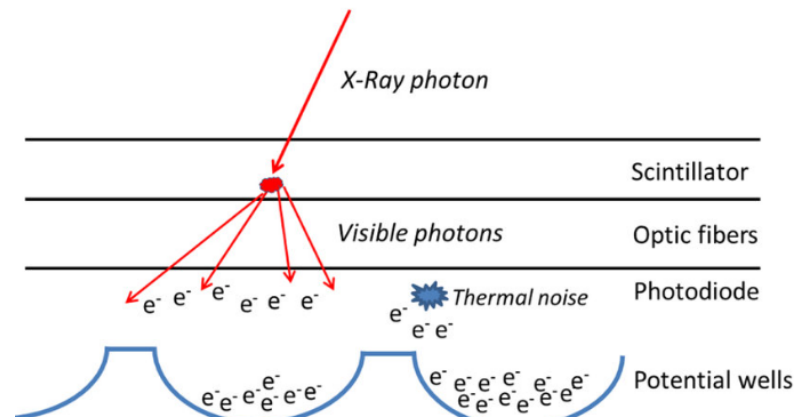


Figure 1.5: Phase Contrast Detector [4]

1.0.4 Voxels

A voxel represents a 3 dimensional cube that determines the length of each grid in the 3 dimensional space [14]. It was invented for the visualization of data in computer graphics, serving the purpose of determining the resolution of an image. The lower the voxel size is, the more cubes can make up the space and therefore one can visualize more precise data points. Depending on a machine's capabilities a minimum voxel size is already established and it allows for volume rendering of 3D objects. A better representation of this concept is shown below:

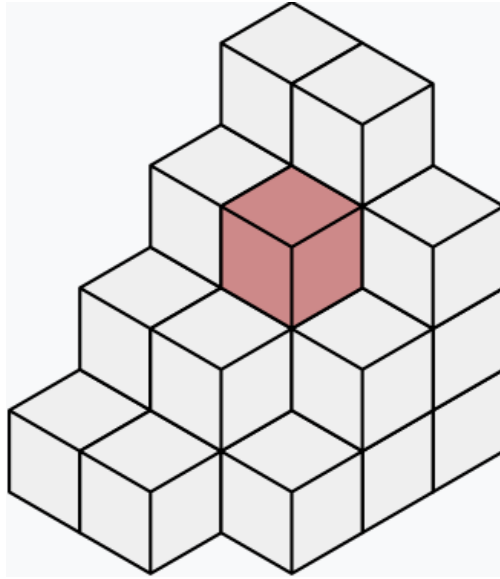


Figure 1.6: Voxel

1.0.5 Hough transform

Once data is properly scanned by any means, the problem of edge detection arises. Being able to reconstruct the edge of each shape within the original image is no easy task and therefore the Hough transform is born out of the need to be able to properly detect boundaries and segment each piece of an image with its proper border. It was developed by Paul Hough in the year 1960 as a need to be able to reconstruct extraneous data points and incomplete data without having to damage the overall image [5]. In its simplest form, the Hough transform takes multiple points in the image space, parametrized by $y_i = mx_i + c$ and changes it to a parameter space with the form $c = -mx_i + y_i$ where its now represented as a line. This can be better viewed with the following figure:

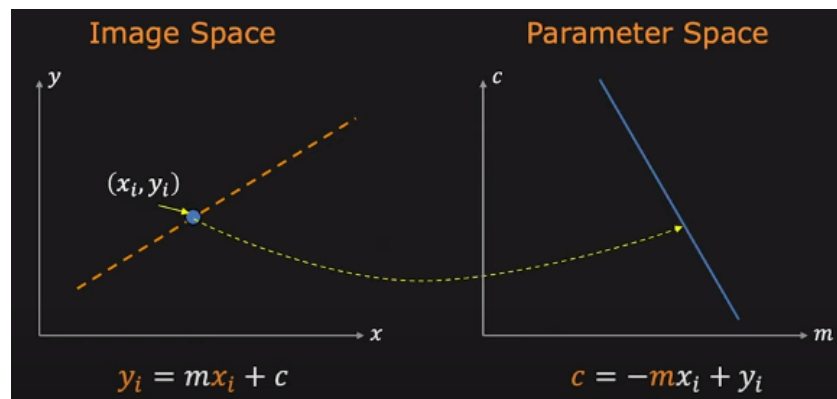


Figure 1.7: Hough Transform [5]

Since x and y values are known it takes all possible values of m and c in the parameter space representing it as a line continuously. If multiple points lie in a connected line in the image space, then that is represented as multiple lines intersect at one value of (m, c) in the parameter space, this can be better viewed with the following figure:

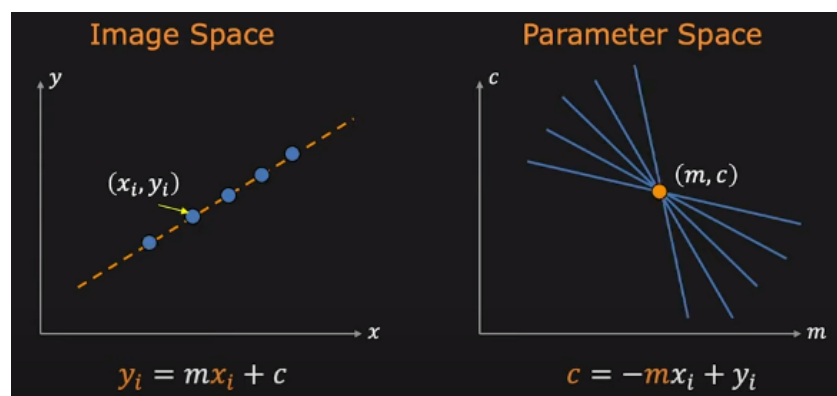


Figure 1.8: Multiple Hough transforms [5]

Points that do not follow a straight line in the image space would be viewed as lines that do not intersect in the parameter space. The way that the line

detection algorithm works in the reconstruction process is quite simple. It involves quantizing the parameter space, that for each point in the image space, the subsequent line that would be in the parameter space has an accumulator array attached to it that increases it by one every time a line passes through those points [5]. Therefore, the intersection points are now determined by the maximum number of votes in a particular space within this accumulator array. This point in particular expresses the (m, c) line value that connects all of the points in the original image space. You can set a limit to how little or big the votes are, in order to see if there is a greater flux of points in the image space or not and also the maximum number of lines you want to view in the parameter space depending on your sample size of points. This can be better seen with the following figure:

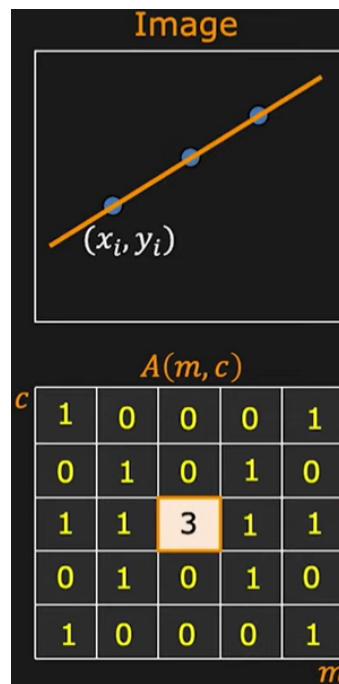


Figure 1.9: Line detection algorithm [5]

Where $A(m, c)$ is the accumulator array program

There is a better parametrization that can be made, the problem with $c = -mx_i + y_i$ for a line is that it goes to infinity and therefore not only is it harder to view patterns, but it consumes more memory computationally. A better parametrization for a straight line is:

$$\rho = x \sin \theta - y \cos \theta$$

Where ρ is the unique distance of $(0, 0)$ to a line that makes a 90° angle and the angle θ is taken from the origin. This is better demonstrated with the following figure.

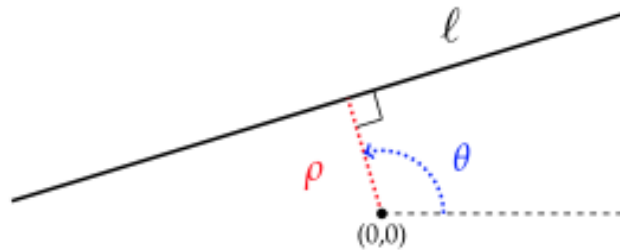


Figure 1.10: Parametrization of a line [6]

Since ρ has a unique distance, this solves the infinite lines problem, having now concrete sinusoidal lines intersecting in a point, this can be seen shown below:

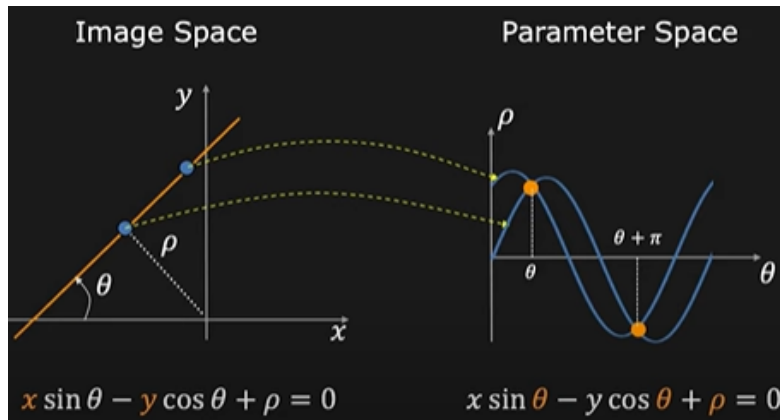


Figure 1.11: Sinusoidal Hough transform [5]

This simple example can be further amplified to 3 dimensions using a point cloud and taking different parametrizations. Instead of returning a line in the parameter space, it returns a plane and the intersections of all of the planes, gives you the equivalence of the (m, b) point in 2D which is represented as a 3 dimensional line that connects all of the points [7].

We do this by represent the line in the form of a vector:

$$\vec{a} + t\vec{b}$$

Where \vec{a} is the point on the line with its x, y, z components and \vec{b} is the direction of the line that is normal to the plane. We can further express \vec{b} as its vertical and horizontal direction components:

$$\vec{b} = \begin{pmatrix} b_x \\ b_y \\ b_z \end{pmatrix} = \begin{pmatrix} \cos\phi\cos\theta \\ \sin\phi\cos\theta \\ \sin\theta \end{pmatrix}$$

The representation of each of the angles is seen in the following figure:

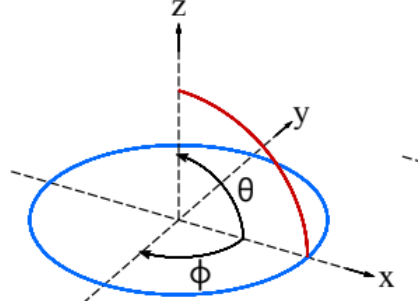


Figure 1.12: Representation of θ and ϕ [7]

we have to restrict \vec{b} in order to obtain a unique solution, we do this by limiting both angles where their value ranges from $0 < \theta \leq \frac{\pi}{2}$ and $-\pi < \phi \leq \pi$. We saw that in figure 7 we described a line that to obtain the parametrization ρ and θ , similarly we have to now describe a plane that is perpendicular to the line as well as the coordinates of the intersection of the line and the plane. For a point $\vec{p} = (p_x, p_y, p_z)$ located in the line, we define the points x' and y' as:

$$x' = p_x \left(1 - \frac{b_x^2}{1 + b_z} \right) - p_y \left(\frac{b_x b_y}{1 + b_z} \right) - p_z b_x$$

$$y' = p_x \left(-\frac{b_x b_y}{1 + b_z} \right) + p_y \left(1 - \frac{b_y^2}{1 + b_z} \right) - p_z b_y$$

We can more precisely see how x' and y' behave in this 3D space with the following graph:

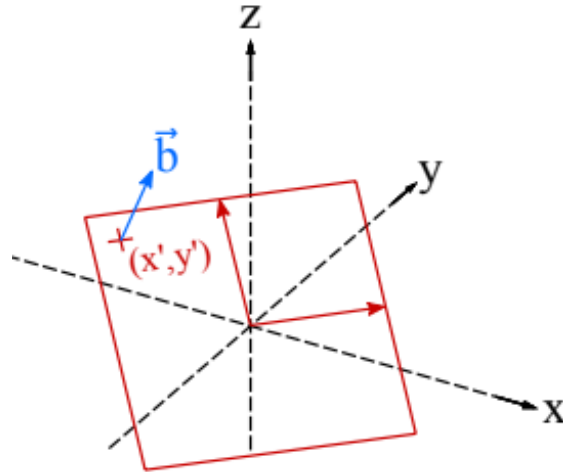


Figure 1.13: The relationship between x' , y' and \vec{b} [7]

The Hough transformation is important, not only because it helps us reconstruct the data, but also because it can give an insight to trends in point clouds that would otherwise be very easily missed, especially when you're dealing with hundred of thousands of points.

The goal of this work is to apply the 3D hough transform to analyze the spatial distribution of pores, such that we can gain greater insight to the possible pottery techniques that were used. These are greatly determined by the intentional trapping of air through specific hand pressure motions. Therefore, an analysis of pore distribution and the straight lines that are obtained in the parameter space of Hough transform, can help us achieve this.

Chapter 2

Methodology

2.0.1 Experimental Set Up

We conducted the experiment at the Laboratorio di Caratterizzazione strutturale e morfologica in CNR-ISASI (Napoli, Italy) using a Bruker Skyscanner X-ray SS1273. The phase-contrast technique used is that of Crystal interferometry using a cone beam for the x-ray source[8]. A diagram of the experimental set up is in Fig. 2. The imaging detector was a Fast readout Low Noise (FReLoN) having a 1k charged-couple device camera. The scintillator screen that was used to turn X-rays to visible lights had a thickness of 50mm having a layer of gadolinium oxysulphide as its photodiode. We obtained data points for 11 samples, however in this thesis we only analyzed 5 samples. They had two resolution analysis, four samples of $10\mu m$ and one sample of $30\mu m$. This was achieved by changing distances. In the first one the source to object distance (SOD) was 30mm, the source to detector

distance (SDD) was 300mm. This gives us the necessary components to calculate the minimum voxel size using the equation $Magnification = \frac{SDD}{SOD}$. With this we obtain a 10X magnification factor. Taking into account that the pixel size of the detector was $100\mu m$ [8] and using the equation:

$$m_{voxel} = \frac{100}{10}$$

We get a voxel size, m_{voxel} , of $10\mu m$.

this means that the minimum resolution is of $10\mu m$, where any measurements below that won't be taken into account or reconstructed fully in the computer.

In the second one, the SOD was 90mm and the SDD was 300mm, giving us a magnification of 3.3X and a Voxel size of $m_{voxel} = 30\mu m$.

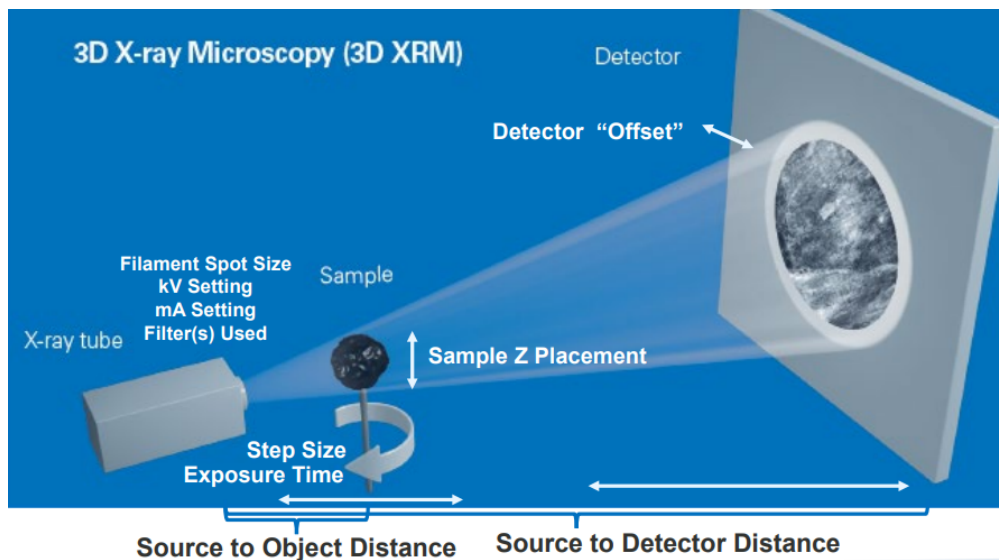


Figure 2.1: Experimental Set Up [8]

Since we are analyzing porous sizes and their distribution, micrometers is a reasonable measurement. This is because our objective is to determine the clay techniques used, which is the intentional trapping of air by hand pressure motions, where unless it is done by high level machinery, it usually falls in the micrometer range. Even though an analysis of pores at the nanometer level would give a greater insight, the natural porosity of clay lies at the nanometer level and that would also cause problems distinguishing which is which. The spatial distribution within the machine is 300mm [8] in each dimension and therefore it does not depend on where we locate the ceramic inside, as we have a high number of scans taken at multiple angles to ensure that the object is fully characterized no matter its position.

The Bruker skyscanner is set up so that the object rotates while the x ray source and detector stay still. This meant that for each of the 11 experimental samples that we scanned, we needed to secure their position in such a way that they would not move during the scan and jeopardize the experiment. We used pieces of foam to place each object in an upright position, depending on all of their varying heights and lengths, different pieces of foam were used. In particular, foam was used because it added very little weight, but also because the attenuation and phase shift experienced by the x ray beam was indistinguishable due to the wave freely passing through the open pores of the foam[15]. We include images of two samples in the figure below, but all of the experimental samples and their dimensions can be seen in the appendix, where at most they had a length of 11 by 11 cm.



Figure 2.2: Ceramic Figures

We chose these fragments, not only because of their cultural heritage, but also because they were significantly smaller than the height requirements by the Skyscanner, which was 30cm by 30cm . This allowed us to have the same source to object distance and source to detector distance for all objects as well as to fully reconstruct the whole image and therefore obtain a better resolution than if we used up all 30cm by 30cm . Equally, the aspect ratio of the beam was of 2.5mm high and 10cm wide, where the ceramic was moved an angle θ after each scan, over all 360° by a distance equal to the height of the X-ray beam. We did two types of resolutions to see if it would have changed the results at the porosity level but also because it meant that it took less time to scan and therefore be able to scan more samples. Around 5000 scans were taken for each sample, giving a total

time of approximately 5 hours per sample analyzed for the $30\mu m$ and around 9 hours per sample for the $10\mu m$. This time depended greatly on the size, shape and density, however most of them fitted within this range. In the appendix there is a clearer table of each sample. The optimum energy levels that we used of the monochromatic plane X-ray wave was $60KeV$. This was an optimum choice because the detector has maximum efficiency at $50KeV$. Equally, when we tried to do energies at $70 - 80KeV$, we found that there was a worse resolution in the images and that was because there appeared to be a greater oscillating behavior of the wavefront phase, which made the intensity peaks recorded by the detector not consistent. Similarly, at lower energies around $40KeV$ and below, there appeared to be blurring effects that didn't aid in the reconstruction, as there was a strong scattering detected, which in some samples didn't allow proper transmission.

2.0.2 Cone Beam Geometry

The way that the X-ray source is achieved is through a cone beam geometry as it was shown in the first figure of this section. This can be seen in the following graphic :

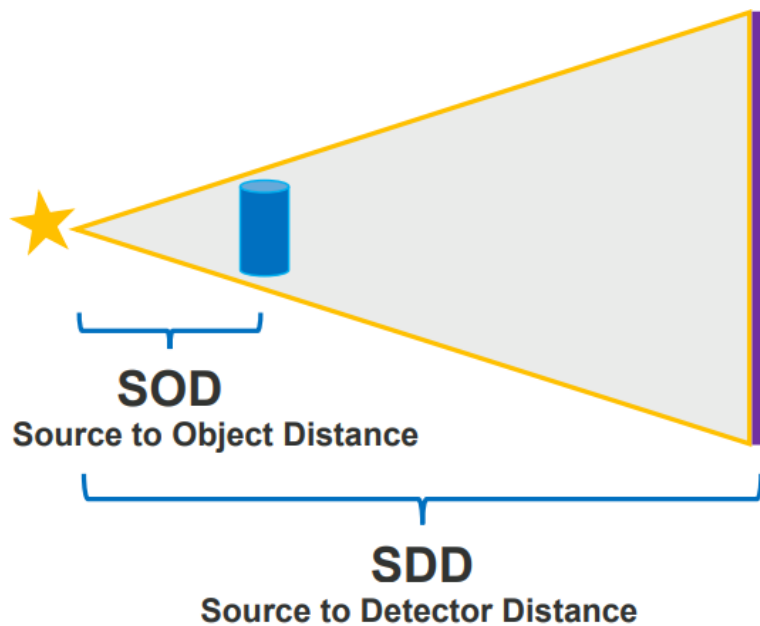


Figure 2.3: Cone Beam X-ray Source [8]

The Cone beam method utilizes the geometry of the system to increase and enhance the x ray in its trajectory towards the detector. Initially, the X ray source, accelerates electrons in order to emit an x ray beam. The way that it works is that inside the tube is a vacuum chamber that has both anodes and cathodes. The anode has an oxidation process and the cathode a reduction reaction. This system maximizes both of these characteristics to first apply a current to the cathode, which makes it release electrons, then apply a potential between the cathode and anode to suddenly accelerate electrons in the direction of the anode and lose energy after coming into contact with the anode [?]. This is done in order to obtain a bremsstrahlung radiation, where the loss of energy that came from these electrons stopping is in the form of X-ray photons. This radiation relies on high currents and potentials in order for the accelerated electrons to be able to knock the electrons

on the anode, producing a transition in energy states that result in a photon X-ray emission. This X ray emission technique gives result to coherent waves. In this experiment, we utilized a monochromatic wave to have a precise energy level throughout the whole experiment.

Once the x ray is produced, it is emitted through a small cylindrical hole to obtain a conical shape. It is important that the object that is being scanned is sufficiently far away for the beam to cover it entirely. Similarly, the detector utilizes to the maximum the geometry of the system in order for it to be placed as far away as possible from the beam source, with the purpose of the beam having the most interactions possible between each of its peaks and troughs of its intensity.

2.0.3 Crystal Interferometry

There are multiple ways to achieve phase contrast techniques, in this lab, in combination with the cone beam set up, we used the crystal interferometry technique. This was used due to the nature of the machine as well as providing relatively low budget with high grades of efficiency [9]. Crystal interferometry divides the beam in two, such that one beam goes through the object, while the other doesn't, making it much more easier to see the contrast of intensity patterns in the detector [2]. An image of this set up is provided in the figure below:

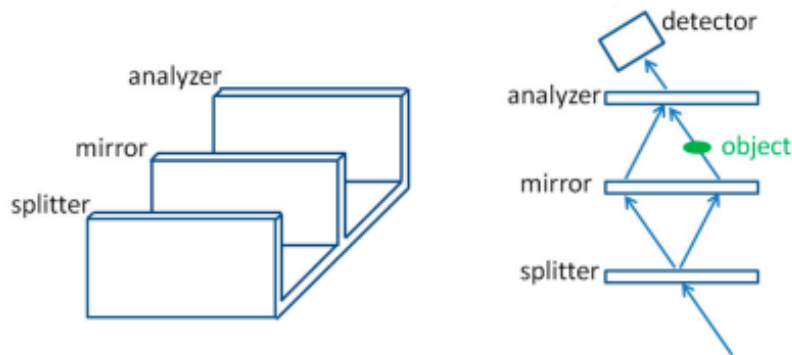


Figure 2.4: Crystal Interferometry [9]

We can see in the figure that it uses the geometry of the system and of the mirrors in order to direct the flow of the x ray and show the differences in the beam paths. We used Silicon for the crystal, as it has no linear or planar imperfections which is relevant to this experiment in order to cause no distortion to the wave by uncontrolled factors [9]. Once the X ray beam enters the splitter, it divides the incident monochromatic beam into 2 coherent waves. Afterwards, both beams start taking opposite directions until they interact with the mirror, causing them to reflect and have convergence. Here we can see that only one of the beams interacts with the object, while the other one doesn't. This is done on purpose, since we know that x ray beams interact differently with different accumulations of particles, this affects the path that the beam takes. After passing the mirror, both coherent waves create a diffraction pattern at the analyzer as they become one beam again. Here the diffraction pattern shows the difference in the beam paths caused by refraction from the object. This technique measures how the phases of the wave changes whilst passing through an object and comparing the phase from the beam that didn't interact with the object. The difference in phases creates

peaks and troughs of intensity that otherwise wouldn't be there, which allows the phase contrast to be examined. By using an entire crystal for this, it meant that adjustments of alignment weren't necessary.

In order to set the incident angle of the X ray, which allows us to determine when the intensity of the diffracted X-ray beam reaches a maximum [?], we used Bragg's condition, as can be better seen below:

$$n\lambda = 2d\sin\theta$$

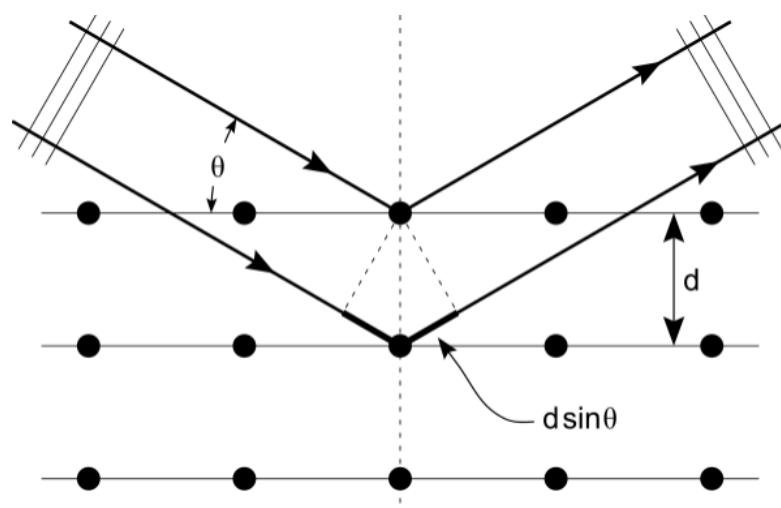


Figure 2.5: Bragg's Condition

Doing this helps to create a coherent scattering of the X-ray wave in order to create a greater interference pattern for the detector to pick up. This in addition with the object to detector distance being greater than the distance from source to object ensured that more defined intensity patterns were recorded.

2.0.4 AVIZO Reconstruction Program

Using the AVIZO-AMIRA program, we could compact all of the 2D scans that were recorded and make them into a 3D virtual object that could be processed for data. One of the functions that AVIZO enables you to do is make a porosity analysis [8]. After various lines of coding that can better seen in Appendix x, you can obtain the spatial distribution of each pore, which is to say its x,y,z coordinates, its area and volume. The coordinates were mapped out using a set 3D scale which determines the origin point and any point away from it has a specific coordinate. The reason AVIZO was used instead of another reconstructing graphics program was that it allows you to create recipes of each coding so that you can replicate the code instantaneously to other samples without having to restart, therefore allowing for faster data analysis in all 11 samples. Equally, it was because it had a faster approach to analyzing pores, while other programs, like Firefly, had a higher difficulty threshold to be able to do pore analysis.

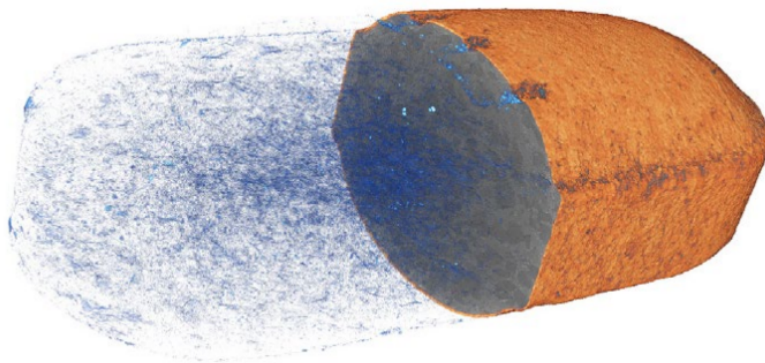


Figure 2.6: Example Of Avizo Reconstruction [8]

2.0.5 Hough Transform

In reference to a paper that also analyzed ancient ceramic porosity through the 3D Hough Transform, we wanted to expand their findings to Ecuadorean ceramics and compare results to find commonalities [6]. We plotted each pore in a 3D graph and used the 3D Hough transform to visualize the patterns of straight lines that the pores make with the hopes to assimilate pore distribution with a clay technique. Each specific points of each pore in a 3D space was transformed into multiple intersecting planes in the parameter space. This intersecting point where the planes met gave back the specific information of the 3D slope line were multiple points are connected into a straight line and that was then graphed in the image space along with all of the pores. As discussed in the introduction, the Hough transform works through a minimum number of votes that the user chooses, which is to say that a minimum number of planes have to intersect before the information of the line is taken and drawn back in the image space. The paper used a minimum number of votes of 18 and graphed 20 potential lines, which we also did. In the paper it was found that by applying different pressure on the clay at the beginning stages before being baked, it conditioned a certain pore distribution on the ceramic, where different techniques on the clay resulted in different Hough transform lines being shown [6]. The paper presented that circular ceramic techniques showed a convergence of Hough lines to single point in the image space, whilst coiling techniques displayed paralel lines in the image space. A better image to convey this information is presented below:

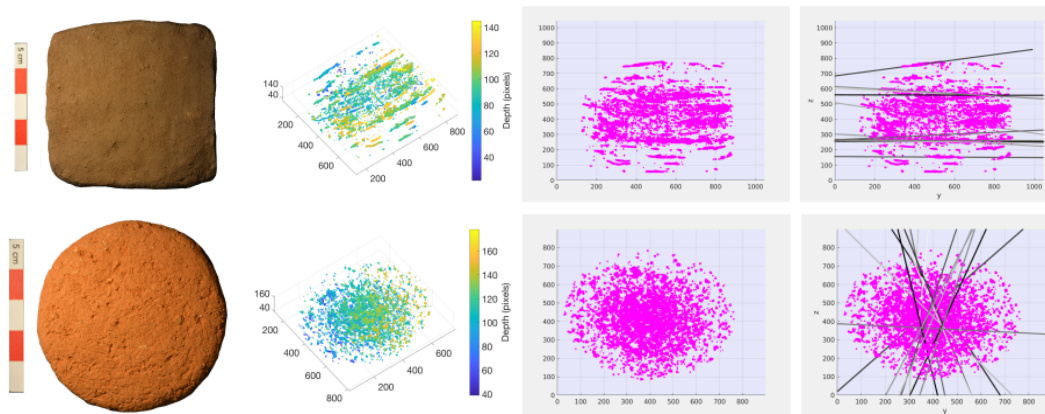


Figure 2.7: Hough lines of Coiling technique (top) and circular techniques (bottom)

We tried to expand on the analysis made by this paper and observe what Hough lines could be deduced on the Pre-colombian ceramic samples found in the Jama Coaque region and potentially deduce a clay technique used by them, or at least rule out techniques that they didn't use. For our results, we used the help of a line detection algorithm, which specifically used the 3D Hough transform in order to visualize our results [7].

Chapter 3

Results

For our results, we are only going to show the most important results of our ceramic pieces. The rest of the results for each ceramic is going to be in the Appendix. Using the AVIZO program we managed to 3D reconstruct the ceramic pieces. The Avizo program gave us, as explained before in the previous section, the volume, area and coordinates (x, y, z) of each pore. In the figure below, we display some reconstructed samples, each with their porosity outlined in different colors. The rest of the samples can be further seen in the Appendix.



Figure 3.1: Reconstructed pieces with visible porosity

The left picture shows only the biggest pores, in various colors. The middle and right picture represents all pores with blueish color having different opacity.

These reconstructions are subject to the error that AVIZO has in its system. As shown in the user's manual of AVIZO [8], it has a 0.25 X Voxel size of error in its reconstruction. So if we have a voxel size of $10\mu m$ then the volume that that cube takes is $1000\mu m^3$ with an error of $15.625\mu m^3$. For a resolution of $30\mu m$, its volume is $27000\mu m^3$ and an error of $421.875\mu m^3$. This error is constant throughout the measurements of all of the pores as it is an intrinsic error that we cannot change.

In order to visualize the make up of pores within the ceramic, we isolated the coordinates of the pores in each of the samples and graphed them using a python code, listed below in the appendix, where the size of each pore was accounted for its volume and its position was accounted by each of its coordinates. Due to the nature of ceramic being a highly porous artefact, as you can see in the blue pores in the previous figure, porosity accounted for more than 90% of each sample. This analysis was done with AVIZO, where it also showed that more than 95% of the pores for all of the samples were connected. Because of this, the number of data points that were collected varied in one way or another. This was divided into two groups. The first group, was the group that did the scan with a resolution of $30\mu m$, where the data could be rendered for all of the 2D scans and gave back less than $100k$ data points. The second group was the group with the highest resolution of $10\mu m$. Here, it proved impossible to reconstruct the whole 3D image, giving more than $1.5m$ data points, making the memory needed to bundle all 2D scans into a 3D image greater than the memory the computer or

the program had to properly render. This led to the computer and the program crashing multiple times, making it unusable due to the limitations of the available equipment. Even when this wasn't an issue and you could obtain porosity results for the $10\mu m$ scans, it gave back millions of porosity data points, which once again the computer and the available equipment couldn't handle to process such large data. The solutions that we implemented for these problems were, either to take less 2D scans for the volume rendering, getting only a segment of the full object, or take at most $250k$ data points, as it seemed that was the cutoff on the computer for data analysis. This solution wasn't detrimental to the experiment because we still had, at minimum, $100k$ data points, which was enough to see potential patterns, even if the whole figure wasn't visualized. In the following figure, we see a couple of different 3D graphs of porous analysis using the python code.

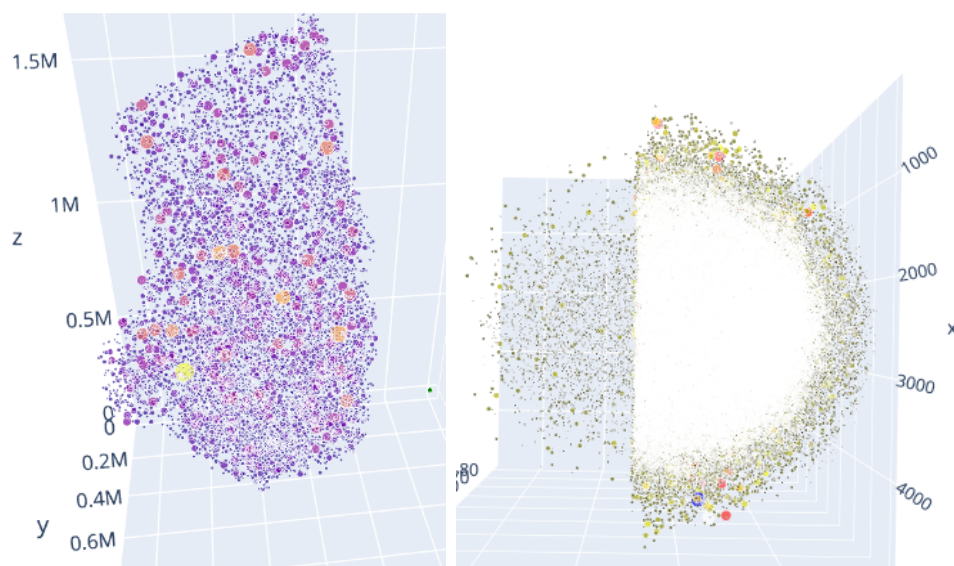


Figure 3.2: Pore Visualization of sample 12 (left) and sample 11(right)

The first image was done with $30\mu m$ and all of its $100k$ pores are graphed while

the second image was done with $10\mu m$ and only $300k$ data points are graphed out of the 1.5 million pores registered. We can see with the first graph, that the pores are evenly distributed, such that they still match the original shape only by looking at the pores. This means that the findings of avizo makes sense, that the pores make up a significant percentage of the original ceramic. The second image only looks a bit incomplete because it has missing data points. It also makes sense that the higher resolution that you have means that the information of pores also increase, finding almost 15 times more pores. Equally, we can visualize that the big pores are relatively small in number compared to the small pores. This can further be seen by doing Histograms for the volume of each pore for both of the above samples.

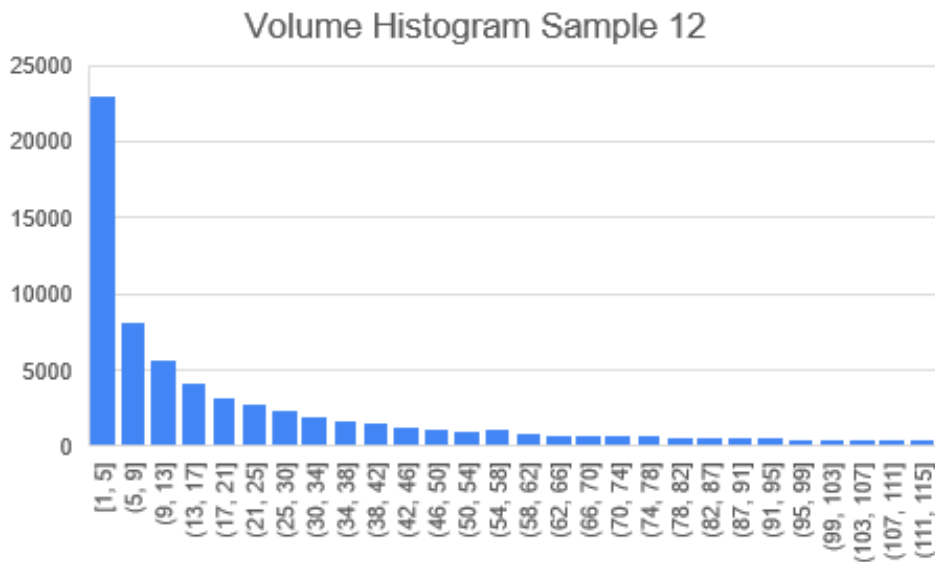


Figure 3.3: Volume Histogram of sample 12 ($27000\mu m^3$)

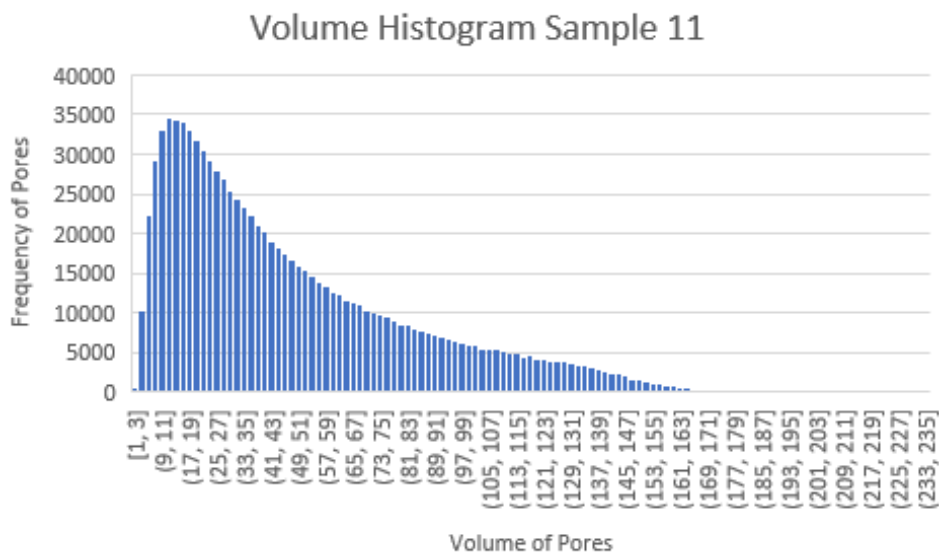


Figure 3.4: Volume Histogram of sample 11 ($1000\mu\text{m}^3$)

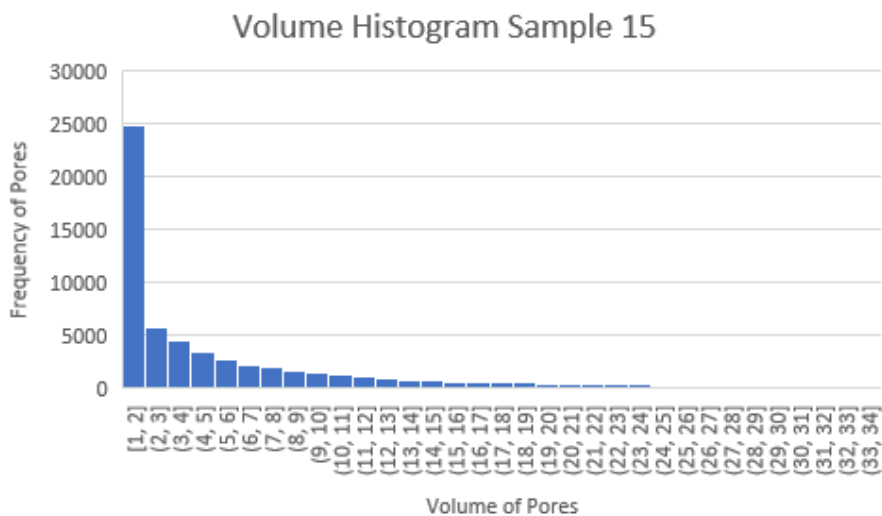


Figure 3.5: Histogram Sample 15 $1000\mu\text{m}^3$

We can see in all of these histograms, as well as the histograms in the Appendix, that the majority of pores are very small pores. The volume of each pore depends on the voxel size which is determined by its resolution. Any number on

the X-axis is a multiple of that number. In the first graph, almost 40% of the data is consumed by pores having a volume of 1 – 9, while the maximum number was 8000. Similarly, in the second graph, more than 60% of the pores have a volume of 1 – 25, while the maximum volume point consisted of 12000. This means that the existence of big pores are definitely an outlier and not only skew the data set, but also represent the intentional concentration of small pores in the construction process of the clay. This can further be represented by a box and whiskers plot of these same data points:

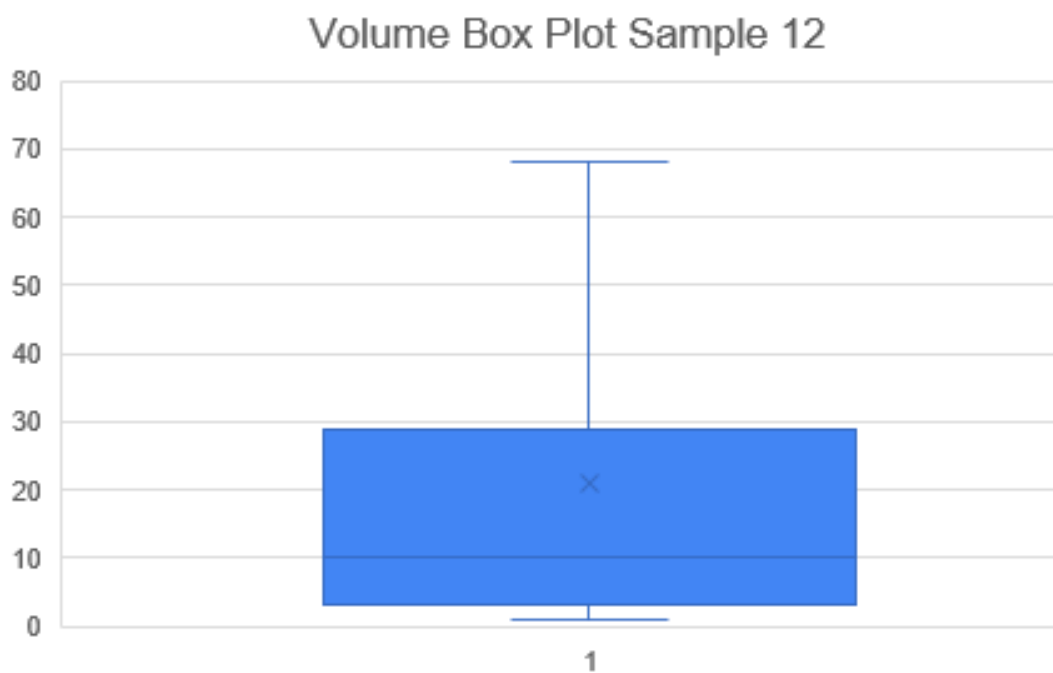


Figure 3.6: Volume Box Plot of sample 12

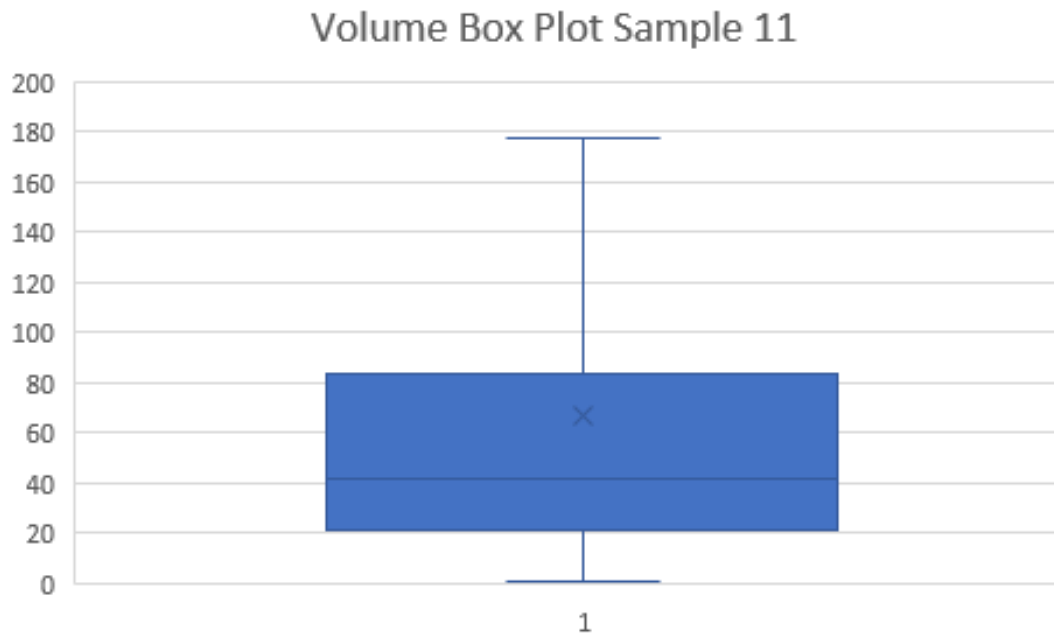


Figure 3.7: Volume Box Plot of sample 11

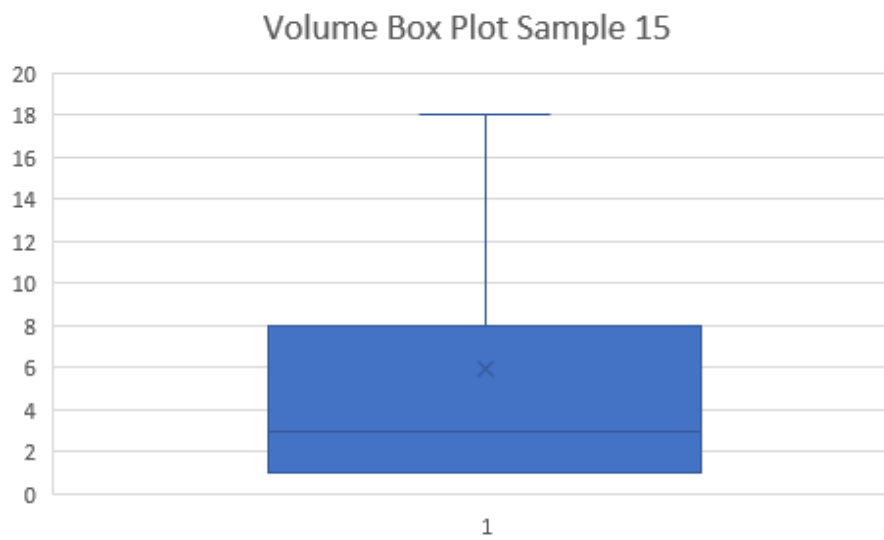


Figure 3.8: Sample 15 box and Whisker Plot

In all figures, as well as all other Box plots in the appendix, it can be observed

that the box is placed significantly closer to the bottom, where it means that the data is skewed to the lower quartiles of data, suggesting in that in both instances the number of big pores on the data were outliers while the smaller pores took up the majority of data.

3.0.1 Hough Lines

In order to obtain the Hough lines, as explained in the methodology section, we implemented the 3D Hough line detection program, where the maximum number of data points that could be inserted were $300k$. this line detection program only gave us a raw image in 2D of these lines and we thought it didn't fully represent the 3D aspect of the figure. Therefore we implemented a python code to visualize these lines. We show 3 different samples in the figures below with their respective ceramic piece next to it, so it can be better visualized. In the first two images we can clearly see very defined parallel lines going in and out of the figure. This agrees with the results from the paper and showcases intentional ceramic techniques displayed in parallel Hough lines as opposed to intersecting Hough lines for different techniques.

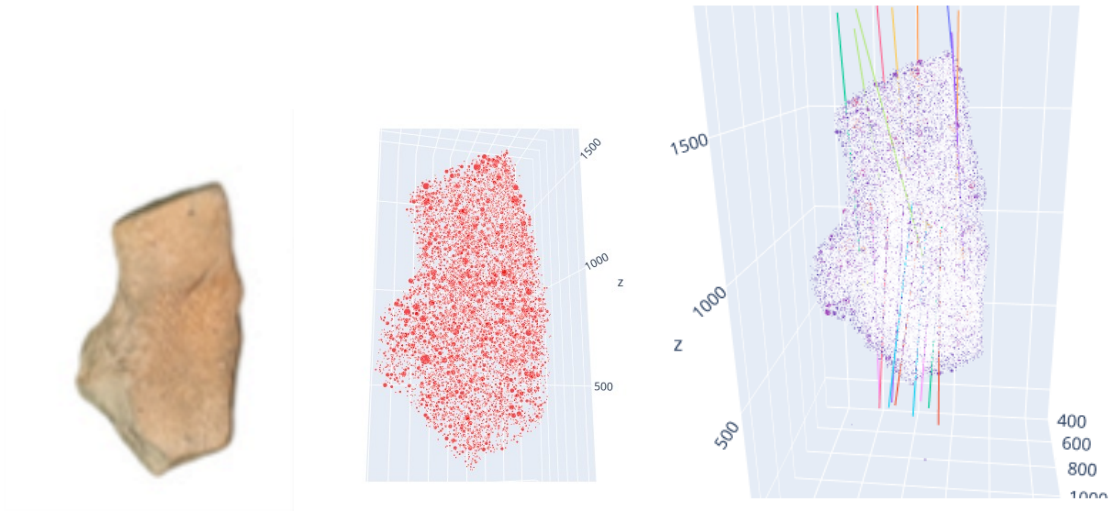


Figure 3.9: Sample 12 Hough Lines

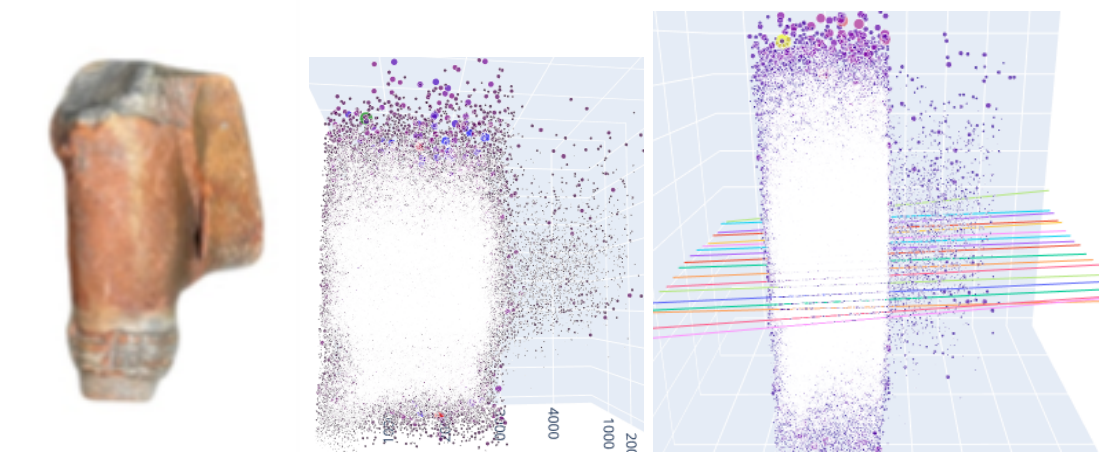


Figure 3.10: Sample 11 Hough Lines

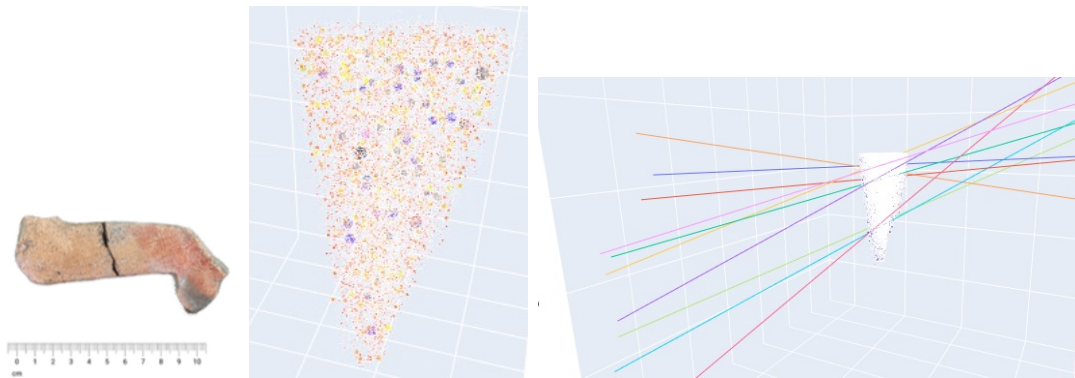


Figure 3.11: Sample 15 Hough Lines

However the parallelism visually within the lines in sample 11 becomes less profound. The majority of the lines can be seen as parallel, however a few lines do cross over and intersect on a couple of points. This can be the result of various reasons. The first is that only a portion of the sample was analyzed. As it can be seen, only a third was reconstructed, the triangular peak at the end of the piece. This was because analyzing all of the porosity points with $10\mu m$ was an impossible task for the available equipment. This could account for some lines overlapping onto others, as the way the sample is constructed is by being bent around. being able to do a full reconstruction of the whole sample could probably reveal a greater insight as to the true nature of the Hough lines. Since it is not clear visually the degree to which these lines are parallel to each other, we decided to run parallelism onto these lines. This means comparing the absolute value of the cosine of the dot product between each pair of lines. Where 1 signifies complete parallelism and 0 signifies completely intersecting lines. We created a box and plot chart to better understand this data.

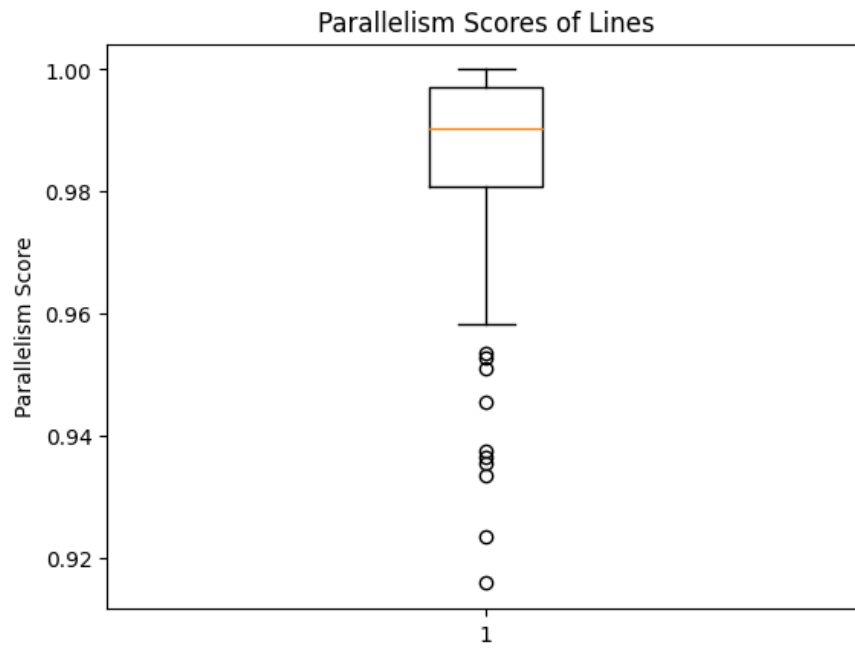


Figure 3.12: Parallelism Sample 12

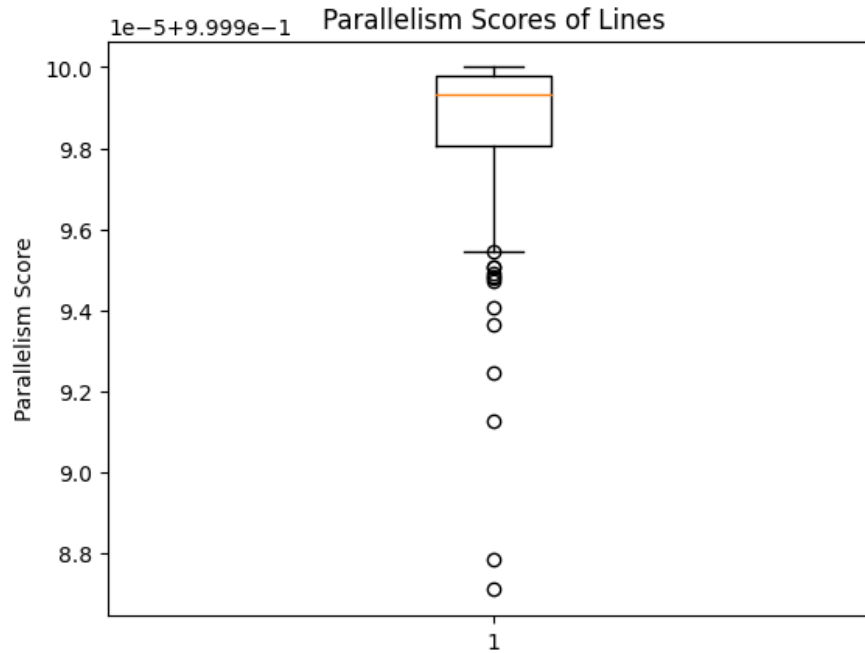


Figure 3.13: Parallelism Sample 11

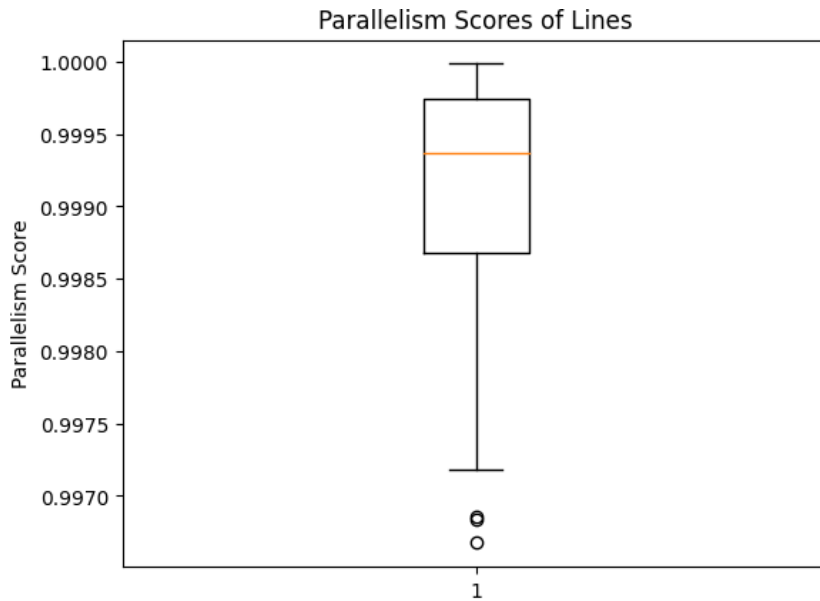


Figure 3.14: Parallelism Sample 15

These box and whisker plots are of the same samples that we used to graph the Hough lines. We can observe that in all 3 graphs the median line (in orange) is significantly closer to 1 than to 0. In sample 12 and 11 the median line is around 0.98, while in sample 15 it is closer to 0.9992. There are outliers in all 3 of these graphs. However, the values of the outliers are still relatively high: 0.91, 0.87 or 0.89 respectively still showcase the degree of parallelism that these lines have. Even if they do intersect, they would only do so over very large distances, which is not relevant for this study as the pores and the ceramic material have a finite distance. Equally, even if visually it appears that some lines overlap, because we are analyzing it in 3 dimensions, these lines exist in different planes and mathematically can still be parallel to one another.

Chapter 4

Conclusions

The X-ray phase contrast technique proved useful in reconstructing samples that had low atomic numbers in the micrometer range when an attenuation contrast would have missed important details. We analyzed 5 different ceramics with two resolutions, one with a voxel size of $30\mu m$ and 4 with a voxel size of $10\mu m$. We could see the difference in the resolution, as we had a 15X difference in the number of porosity within samples. Even with these difference, all samples showed an abundant of low porosity, where at least 60 percent account for volumes between 1 – 50. This in comparison with the biggest pores ranging from 4000 – 12000 and accounted for less than 3 percent of all pores.

The Hough transform successfully allowed us to graph lines obtained in the parameter space onto the image with all of the pores. This allowed us to properly view how the pores are connected with each other and if they present a specific pattern with the lines, or if the pores give back random lines. We discovered that

in all of the samples there was a strong correlation for parallel lines, instead of intersecting lines. Equally, for the box and plot analysis of parallelism, we found that all median lines skewed towards the upper quartile, with values higher than 0.9, which shows that the majority of lines have a strong parallel nature between each other. Not only were there few outlier points, but their lowest value was 8.7, which still represents a parallel nature for the limited size of the ceramic, as the lines would have to stretch farther than the ceramic to intersect. This agrees with the result obtained from the papers researched for this thesis, which showcase a strong correlation of parallelism with a coiling technique. Due to the low number of samples that were analyzed, it is not enough to properly say that in fact these civilizations used these coiling techniques for all their ceramics or that there couldn't exist other techniques that also present parallel lines. However, it can give an insight as to what techniques were not used, which is the case for intersecting Hough lines and circular patterns. The abundance of small pores, could potentially indicate a deliberate effort of making their ceramics as refined as possible, getting rid of as many big pores. This could also be due to a number of samples but this research is also ongoing.

These results can be improved in future researches by having a greater computational capacity in order to be able to process and render all of the data samples with greater resolution. Equally, the data can be better analyzed with a lower voxel size, adjusting the SDD and SOD distances, which would also give better measurements. Similarly, implementing a code that will render more than 300k data points for the Hough lines, would equally give greater correlations between data sets.

The possible errors in our analysis are made from the AVIZO reconstruction software and coordinate, area and volume data. Avizo is not perfect, and as such could have included data that is not porous or give wrongful coordinates. The error in Avizo is 0.25X Voxel size, which for both the $10\mu m$ and $30\mu m$ would give a percentage error of 0.0156. Even with this error, we could still see very clearly the reconstructed image with all of its characteristics, especially its pores. Even if there were errors in the reconstruction it wasn't impactful for the data analysis. The coordinate, area and volume data could be a greater source of error, as you can see in the reconstructed images, pores aren't always spherical, however in order to visualize them better, AVIZO, in its data analysis, plotted each pore as a sphere where its size was proportional to the volume and area given by the program. This could produce errors in the shape of certain pores. However, the sphere was fitted in the center of mass of each of the pore, reducing each error. Since the majority of pores were very small, the center of mass was more than enough to accurately obtain the position of each pore, where the big pores also accounted for a proportional size of sphere.

Bibliography

- [1] S D Auweter, J Herzen, M Willner, S Grandl, K Scherer, F Bamberg, M F Reiser, F Pfeiffer, and K Hellerhoff. X-ray phase-contrast imaging of the breast—advances towards clinical implementation. *The British Journal of Radiology*, 87(1034):20130606, February 2014.
- [2] Philip J. Withers, Charles Bouman, Simone Carmignato, Veerle Cnudde, David Grimaldi, Charlotte K. Hagen, Eric Maire, Marena Manley, Anton Du Plessis, and Stuart R. Stock. X-ray computed tomography. 1(1):18.
- [3] Nenah Sylver. Healing with electromedicine and sound therapies from: The rife handbook of frequency therapy and holistic health an integrated approach for cancer and other diseases 5 th edition second printing. pages 919–955, 07 2022.
- [4] P Allé, Wenger Emmanuel, S Dahaoui, D Schaniel, and Claude Lecomte. Comparison of ccd, cmos and hybrid pixel x-ray detectors: Detection principle and data quality. *Physica Scripta*, 91:063001, 06 2016.

- [5] First Principles of Computer Vision Shree Nayar. Hough transform boundary detection, March 2021.
- [6] V.L. Coli, L. Gomart, D.F. Pisani, S. Cohen, L. Blanc-Féraud, J. Leblond, and D. Binder. Microcomputed tomography for discriminating between different forming techniques in ancient pottery: New segmentation method and pore distribution recognition. *Archaeometry*, 64(1):84–99, February 2022.
- [7] Christoph Dalitz, Tilman Schramke, and Manuel Jeltsch. Iterative Hough Transform for Line Detection in 3D Point Clouds. *Image Processing On Line*, 7:184–196, 2017. <https://doi.org/10.5201/ipol.2017.208>.
- [8] Thermofisher Scientific. User’s guide avizo software 2019, April 2019.
- [9] Siwei Tao, Congxiao He, Xiang Hao, Cuifang Kuang, and Xu Liu. Principles of Different X-ray Phase-Contrast Imaging: A Review. *Applied Sciences*, 11(7):2971, March 2021.
- [10] María José Morillo, Florencio Delgado, and Mateo Subía. Acercándose al pasado, una aproximación arqueológica al programa de vinculación. *Esferas*, 4:54–69, April 2023.
- [11] Jens Als-Nielsen and Des McMorrow. *Elements of modern X-ray physics*. Wiley, a John Wiley & Sons, Ltd Publication, Chichester, West Sussex, second edition, reprinted with revisions and corrections edition, 2017.
- [12] Marco Endrizzi. X-ray phase-contrast imaging. *Nuclear Instruments and Methods in Physics Research Section A: Accelerators, Spectrometers, Detectors and Associated Equipment*, 878:88–98, January 2018.

- [13] Vito Mocella, Emmanuel Brun, Claudio Ferrero, and Daniel Delattre. Revealing letters in rolled Herculaneum papyri by X-ray phase-contrast imaging. *Nature Communications*, 6(1):5895, January 2015.
- [14] A.L. Goertzen, F.J. Beekman, and S.R. Cherry. Effect of voxel size in CT simulations. In *2000 IEEE Nuclear Science Symposium. Conference Record (Cat. No.00CH37149)*, volume 3, pages 20/93–20/97, Lyon, France, 2000. IEEE.
- [15] Redouane Meftah, Jeroen Van Stappen, Sylvain Berger, Gary Jacques, Jean-Yves Lalue, Paul-Henri Guering, Luc Van Hoorebeke, and Veerle Cnudde. X-ray Computed Tomography for Characterization of Expanded Polystyrene (EPS) Foam. *Materials*, 12(12):1944, June 2019.

Appendix A

Histogram graphs of ceramic samples

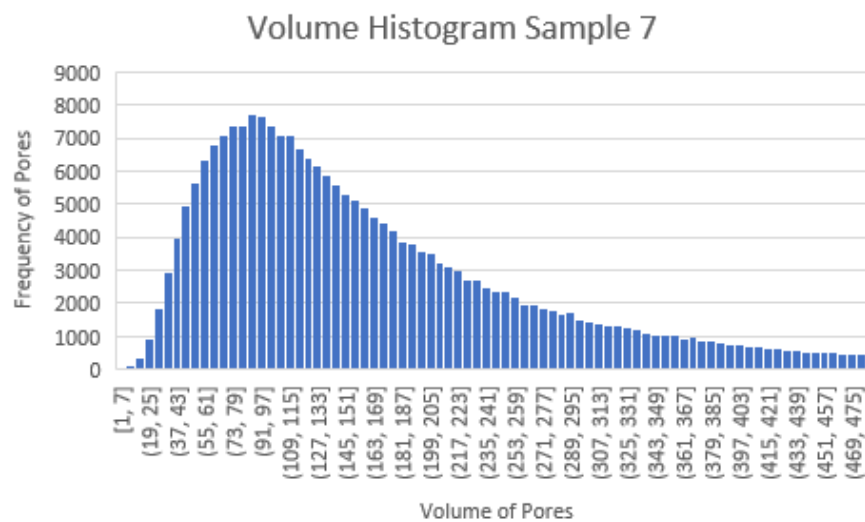


Figure A.1: Histogram Sample 7

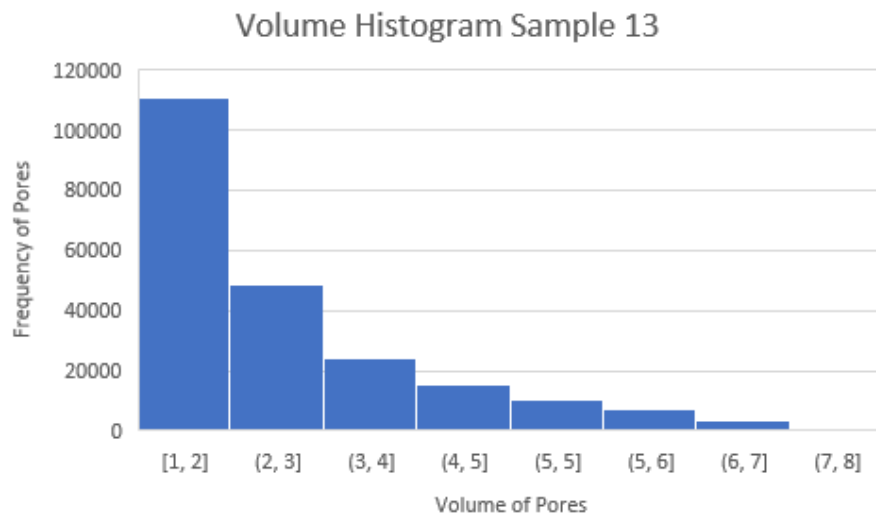


Figure A.2: Histogram Sample 13

Appendix B

Box and whisker plots of ceramic samples

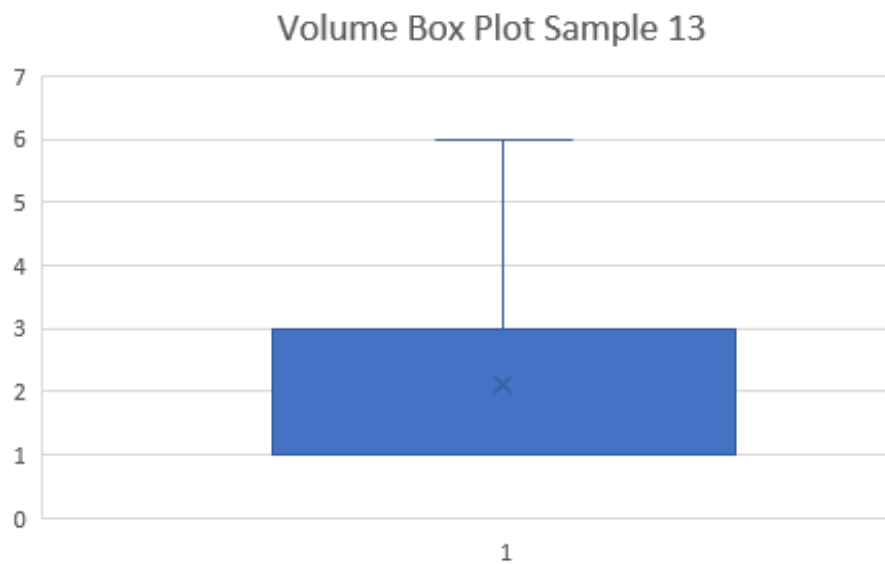


Figure B.1: Histogram Sample 13

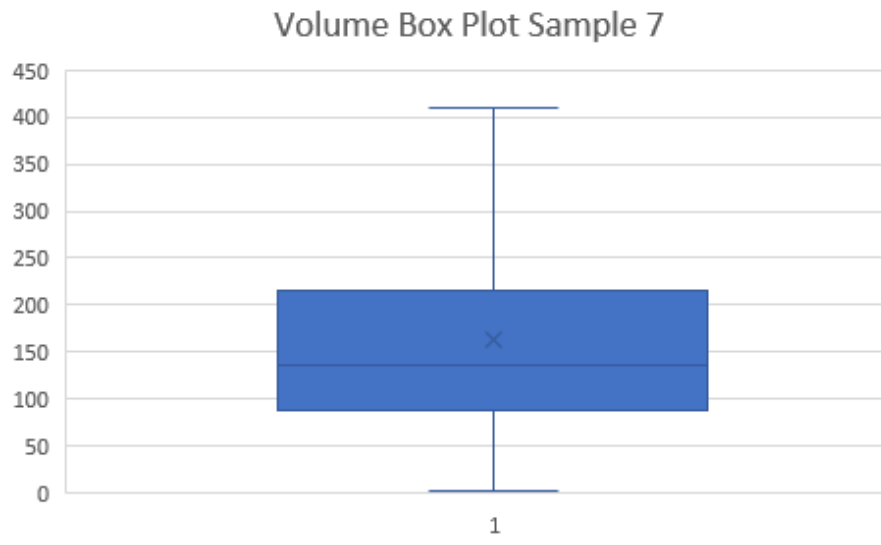


Figure B.2: Histogram Sample 7

Appendix C

Hough lines and parallelism



Figure C.1: Ceramic sample 7

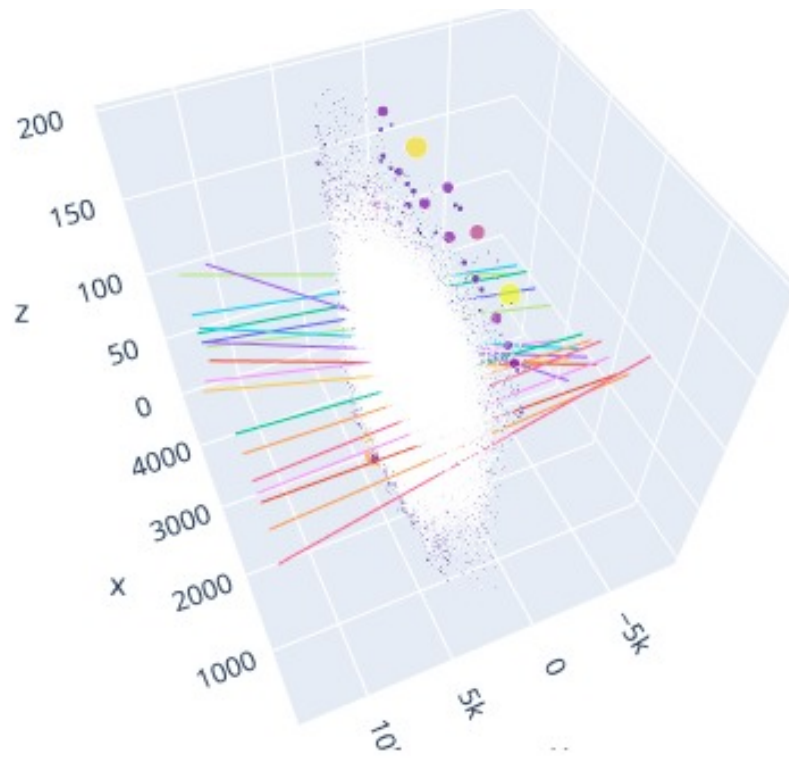


Figure C.2: Hough lines sample 7

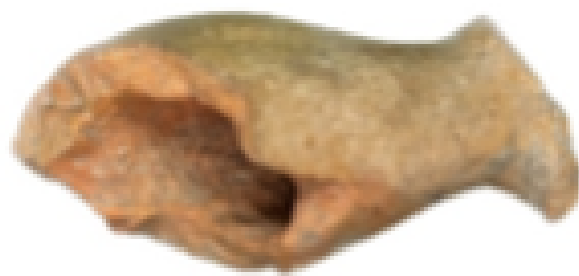


Figure C.3: Ceramic Sample 13

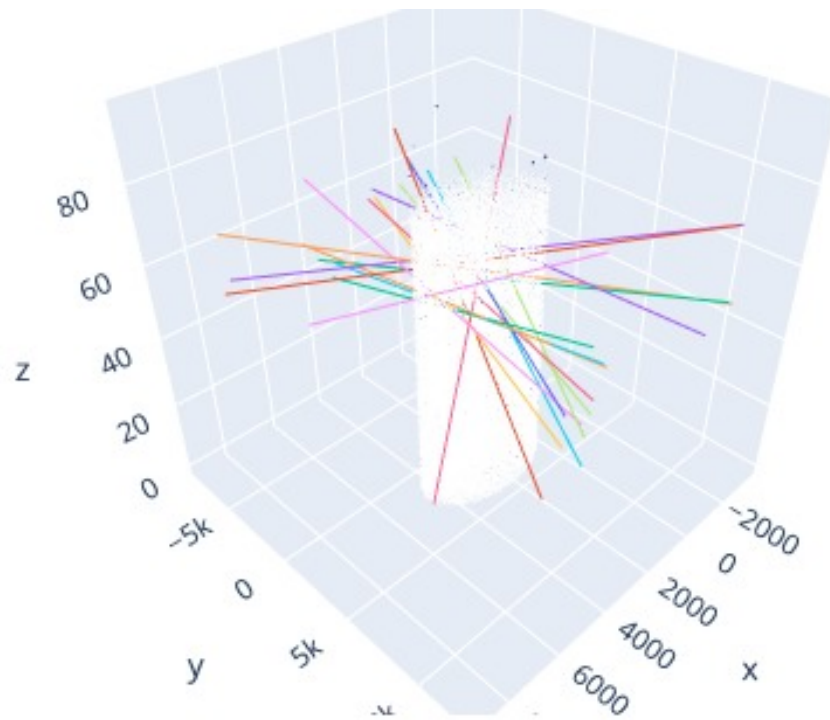


Figure C.4: Hough lines sample 13

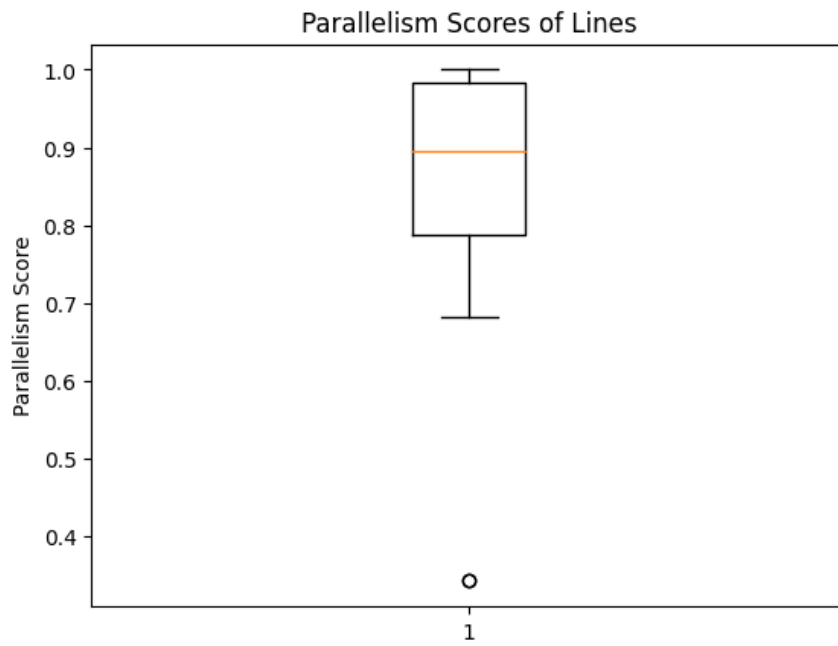


Figure C.5: Parallelism Sample 13

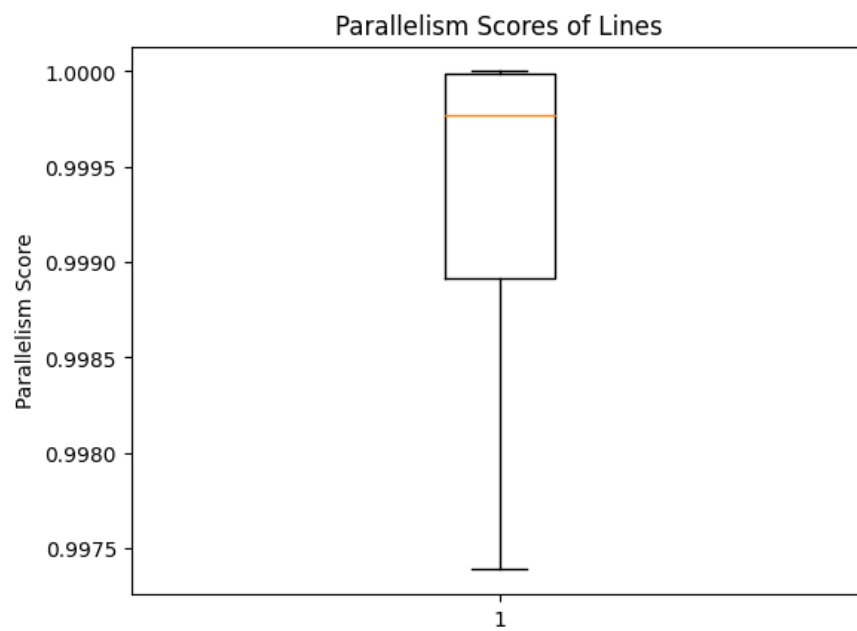


Figure C.6: Parallelism Sample 7